Exploring the potential of coherent imaging using photonic lanterns with beam combiners

Yoo Jung Kim[a], Michael P. Fitzgerald[a], Jonathan Lin[a], Steph Sallum[b], Yinzi Xin[c], Nemanja Jovanovic[c], Sergio Leon-Saval[d], Christopher Betters[d], Pradip Gatkine[c], Olivier Guyon[e], Julien Lozi[e], Dimitri Mawet[c], Barnaby Norris[d], and Sebastien Vievard[e]

[a]Department of Physics and Astronomy, University of California, Los Angeles, 475 Portola Plaza, Los Angeles, CA 90095, USA
[b]Department of Physics and Astronomy, University of California, Irvine, 4129 Frederick Reines Hall, Irvine, CA 92697, USA
[c]Department of Astronomy, California Institute of Technology, 1200 East California Boulevard, Pasadena, CA 91125, USA
[d]School of Physics, University of Sydney, Camperdown NSW 2006, Australia
[e]Subaru Telescope, National Observatory of Japan, HI 96720, USA

ABSTRACT

Photonic Lanterns (PLs) are tapered waveguides that can efficiently couple multi-mode telescope light into a multi-mode fiber entrance at the focal plane and coherently convert it into multiple single-mode beams. Each SMF samples its unique mode (lantern mode) of the telescope light in the pupil, analogous to subapertures in aperture mask interferometry. In this study, we show the concept and potential of coherent imaging with PLs. It can be enabled by interfering SMF outputs and applying path length modulation, which can be achieved using a photonic chip beam combiner at the backend (e.g., the ABCD beam combiner). Using numerically simulated lantern modes of a 6-port PL, we calculate interferometric observables for various input scenes. Our simulated observations suggest that PLs may offer significant benefits in the photon-noise limited regime and for resolving small-scale ($< \lambda/2D$) asymmetries.

Keywords: photonic lantern, beam combiner, coherent imaging, interferometry, photonics, high angular resolution

1. INTRODUCTION

Photonic Lanterns (PLs) are tapered waveguides that efficiently convert mult-modal light into single moded beams.[1,2] They have multimode or few-mode fiber (MMF or FMF) at the input entrance and multiple single-mode fibers (SMFs) at the other end. Figure 1 shows a schematic diagram of a 6-port PL. The FMF end of the PL is placed in the focal plane, coupling the AO-corrected telescope light. Then the light gets confined within the cores as it propagates through the lantern transition. Therefore, a PL splits a few-moded wavefront into a few single-moded beams, each in an individual SMF. The outputs confined in the SMFs are highly stable due to the spatial filtering nature of the SMF,[3] suitable for observations that require high fidelity.

PLs do not split fluxes equally to each SMF output but the relative fluxes in the SMFs depend on the input wavefront. Therefore, PLs can be used as a focal-plane wavefront sensor.[4,5] PLs can also be used for spectroastrometry, by sensing wavelength-dependent relative intensities in output SMFs.[6,7] If the PL were mode-selective,[8] it could be used as a nuller that suppresses the on-axis starlight while coupling the off-axis light from a companion source.[9]

Here, we explain the concept of interfering the SMF outputs to exploit the coherence properties of a PL that enables coherent imaging with PLs at small angular scales, presented in Kim et al., submitted.[10] This can be realized by feeding SMF outputs into a backend photonic integrated circuit beam combiner.

Further author information:
Yoo Jung Kim: E-mail: yjkim@astro.ucla.edu

Techniques and Instrumentation for Detection of Exoplanets XI, edited by Garreth J. Ruane, Proc. of SPIE Vol. 12680, 126800K · © 2023 SPIE
0277-786X · doi: 10.1117/12.2677054

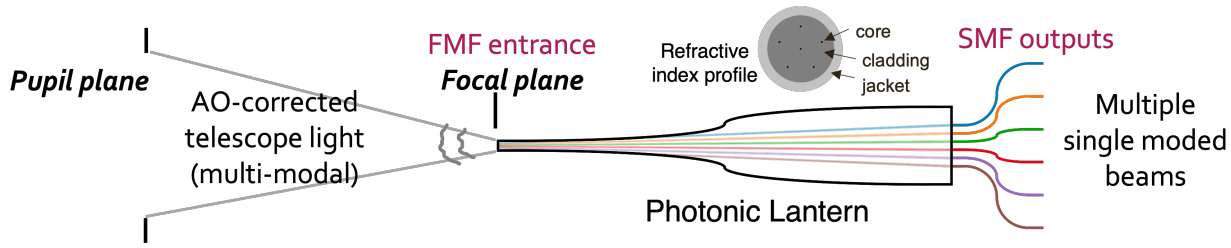

Figure 1. A schematic diagram of a standard 6-port PL. The telescope light is injected into the PL at the focal plane through the FMF end, propagates through the PL and becomes confined in the SMFs. The SMF outputs can be directed to photonic chips or other devices and then to the detector. A cross-section of the PL at the few-core fiber (FCF) end is shown in the upper right.

2. CONCEPT OF PL COHERENT IMAGING

In classical interferometry, pairs of apertures are interfered to measure the corresponding fringe visibility. For instance, non-redundant masking technique[11–14] uses a pupil mask with a several machined holes designed so that the baselines formed by each pair correspond to unique spatial frequencies. Similarly, the light in an output SMF represents the telescope light filtered by a unique effective aperture determined by the properties of the lantern.

For a radially symmetric step-index fiber, the linearly polarized modes (LP modes) describe the propagation eigenmodes. For example, a 6-port PL supports 6 modes of propagation and its propagation eigenmodes at the PL entrance can be approximated to the six LP modes, LP_{01}, $\mathrm{LP}_{11(a,b)}$, $\mathrm{LP}_{21(a,b)}$, and LP_{02} (upper left of Figure 2). After the lantern transition, the corresponding modes in the output end are described as the upper right panel in Figure 2. See section 4.1 for simulation parameters of the 6-port PL. Colors represent the phase and saturation indicates the amplitude. We can think of another mode basis, the Photonic Lantern Principal Modes (PLPMs; "lantern modes").[4,10] PLPMs are defined as an orthogonal superposition of the LP modes that maps to one SMF output. Numerically, these modes at the lantern entrance can be calculated by backpropagating the fundamental modes in the SMF outputs (lower right in Figure 2) to the entrance (lower left in Figure 2).

Backpropagating the PLPMs at the lantern entrance (at the focal plane) to the pupil plane, the pupil plane PLPMs can be found. These can be interpreted as effective apertures (left panel in Figure 3) seen by the lantern — the pupil-plane wavefront that matches the pupil plane PLPM i will couple into the PL and end up in the $i-$th SMF in the output. Thus the complex amplitudes in different SMF outputs represent the light from different effective apertures.

Each mode amplitude distribution peaks in different locations at the pupil, implying that each SMF preferentially samples more light at specific locations, similar to a "subaperture" in aperture masking interferometry (middle and right panels in Figure 3). Interfering a pair of output SMFs (i and j) provides access to interferometric properties of the input scene — the PL visibility.[10]

$$\text{PL visibility}: \mathcal{V}_{ij} = \frac{2\iint_{\infty}^{\infty} J_{\mathrm{p}}(u,v)\ (P_{\mathrm{eff},j} \star P_{\mathrm{eff},i})(u,v)dudv}{\iint_{\infty}^{\infty} J_{\mathrm{p}}(u,v)\ (P_{\mathrm{eff},i} \star P_{\mathrm{eff},i} + P_{\mathrm{eff},j} \star P_{\mathrm{eff,j}})(u,v)dudv} \tag{1}$$

Here the integral is over the $u-v$ plane, the distances between two spatial points measured in wavelengths. J_{p} represents the mutual intensity (panel (b) of Figure 4), which corresponds to the Fourier transform of the source intensity distribution (panel (a)) by the Van Cittert-Zernike theorem. $\mathrm{P}_{\mathrm{eff,i}}$ denotes the effective pupil function of the $i-$th output and the star symbol represents the two-dimensional cross-correlation. There are 15 unique visibilities for a 6-port PL. Equation (1) shows that the PL visibilities are proportional to the product of the mutual intensity in the pupil plane and the cross-correlation of the effective pupil functions, integrated over the $u-v$ plane. Thus the cross-correlation of effective pupil functions serve as a weight function of the mutual intensity at the pupil. The panel (d) of Figure 4 visualizes the interpretation of PL visibilities. For comparison, the aperture masking interferometry analog is shown in the panel (c), the case where masks are placed at locations where amplitudes of PL effective pupil functions are maximized (right panel in Figure 3).

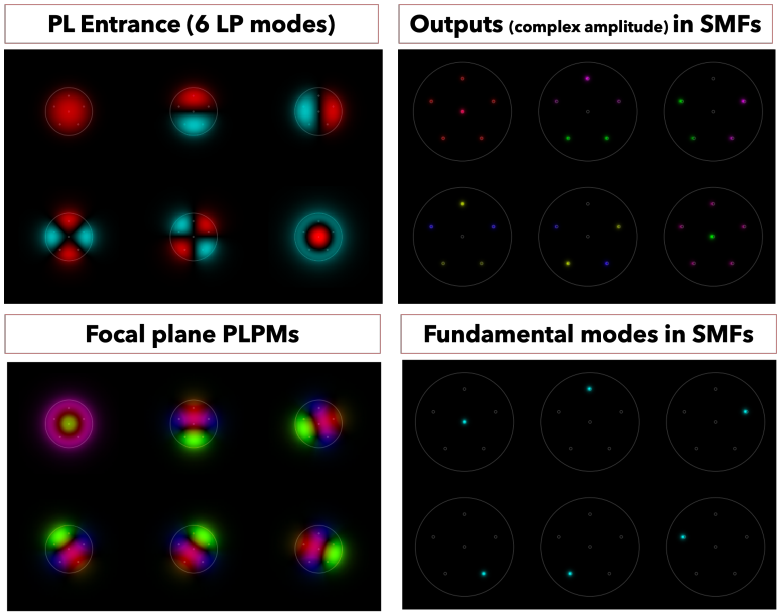

Figure 2. (Top) The six supported LP modes of a 6-port PL at the entrance (left) and the modes propagated to the output end (right). Since the light propagation is linear in complex amplitudes, we another mode basis can be defined that maps to one SMF output: the PL principal mode (PLPM). (Bottom) The six PLPMs of the 6-port PL at the PL entrance (left) and at the output end (right).

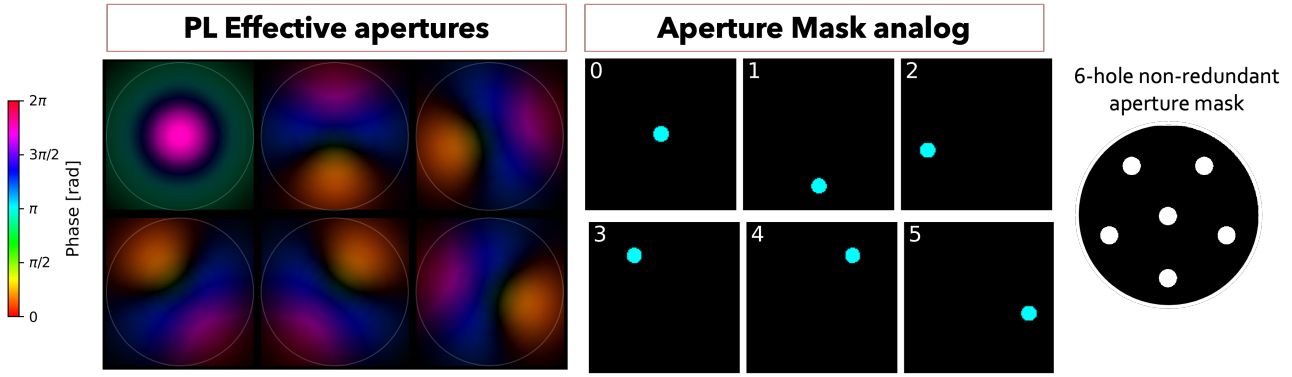

Figure 3. ((Left) The effective apertures of the 6-port PL, found from pupil plane PLPMs. (Right) A 6-hole aperture mask analog of the lantern effective apertures.

To measure PL visibilities, beams from the lantern outputs should be coherently combined with path length difference. The pairwise ABCD beam combination scheme[15,16] is conceptually straightforward and a photonic implementation has been successfully deployed within the GRAVITY instrument at the Very Large Telescope Interferometer.[17] An ABCD beam combiner receives two inputs (E_i, E_j) and provides four outputs ($I_{ij,A}$,$I_{ij,B}$,$I_{ij,C}$,$I_{ij,D}$), each resulting from a pairwise combination with phase difference of multiples of 90 degrees. The complex visibility can be determined from the four outputs such as:

$$\mathcal{V}_{ij} = \frac{(I_{ij,A} - I_{ij,B}) + (I_{ij,C} - I_{ij,D})i}{I_{ij,A} + I_{ij,B} + I_{ij,C} + I_{ij,D}}. \tag{2}$$

Note that this assumes an ideal case neglecting factors like instrumental phase shift, instrumental contrast, intensity losses, unequal splitting ratios, chromaticity, and polarization. We defer the consideration of these to future work.

To obtain all the 15 unique visibilities for our 6-port lantern, 15 ABCD beam combiners are needed for

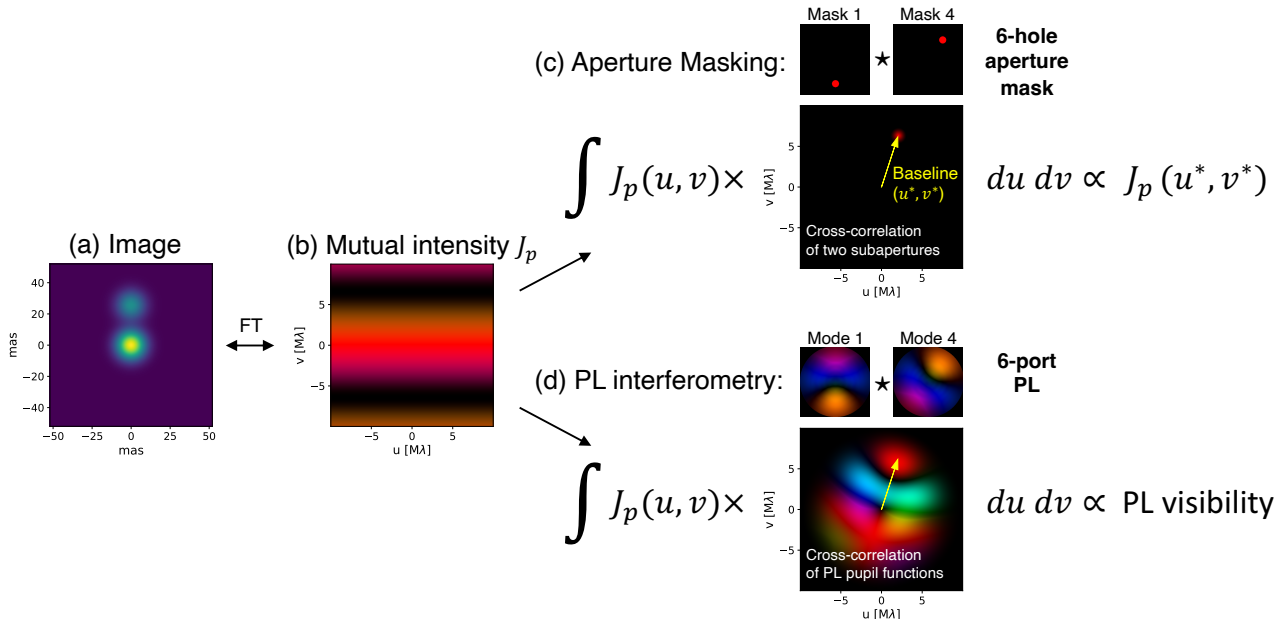

Figure 4. A concept diagram of PL interferometry, showing physical interpretation of PL visibilities. (a) An example image of a binary star system with separation 25 mas and flux ratio 0.5, convolved by a $\lambda/2D$ Gaussian beam for display. (b) Mutual intensity in the pupil plane $J_p(u,v)$, which is the two-dimensional Fourier transform of the image in the left. (c) Cross-correlation of two subapertures of a 6-hole aperture mask. The hole locations are defined as the peaks in the PL pupil functions. The cross-correlated aperture functions are well-localized at some (u,v), so the visibility measured from light transmitted by these two apertures approximately equals to the visibility at this (u,v) baseline. (d) Cross-correlation of two PL pupil functions of a 6-port PL. The cross-correlated pupil functions is extended but has a defined blob at the (u,v) location in the aperture mask case. Visibilities we can measure from a PL correspond to the product of $J_p(u,v)$ and the cross-correlated pupil function integrated over the $u-v$ plane.

pairwise beam combination, leading to 60 outputs in total. Generally, a pairwise beam combination of an N-port PL will require $N(N-1)/2$ beam combiners and will result in $2N(N-1)$ outputs. Figure 5 shows a conceptual diagram of a pairwise beam combiner for a 6-port PL.

3. COMPARISON BETWEEN PL VISIBILITIES AND SEPARATED-APERTURE VISIBILITIES

To understand properties of PL visibilities, we calculated those for simple models: a uniform circular disk model, binary models (Figure 6), and ring models (Figure 7). For comparison with separated-aperture visibilities, an aperture masking interferometry analog of a mask configuration in Figure 3 is considered. All baselines are non-redundant in this configuration.

Similar first-order responses at small scales In Figure 6, the behaviors of squared visibilities as increasing the disk radius or binary separation are similar at angular scales $< \lambda/2D$. This is because mutual intensity at the pupil plane (J_p) changes gradually over the $u-v$ plane for small angular size objects, slower than the variation of the cross-correlated pupil functions over the $u-v$ plane.

Sensitivity to asymmetries and phase angle degeneracy In Figure 6(b), the squared visibilities of binary models for two position angles (0 and 180 degrees) are shown. While squared visibilities for aperture masks for the two position angles are equal to each other, the PL squared visibilities for the two position angles are different — the case for zero position angle having larger signals than for the 180 degrees position angle. Moreover, in Figure 7 the difference between the interferometric observables for the symmetric and asymmetric ring models are more significant for the PL visibilities than the aperture masking interferometry analog. This is because the

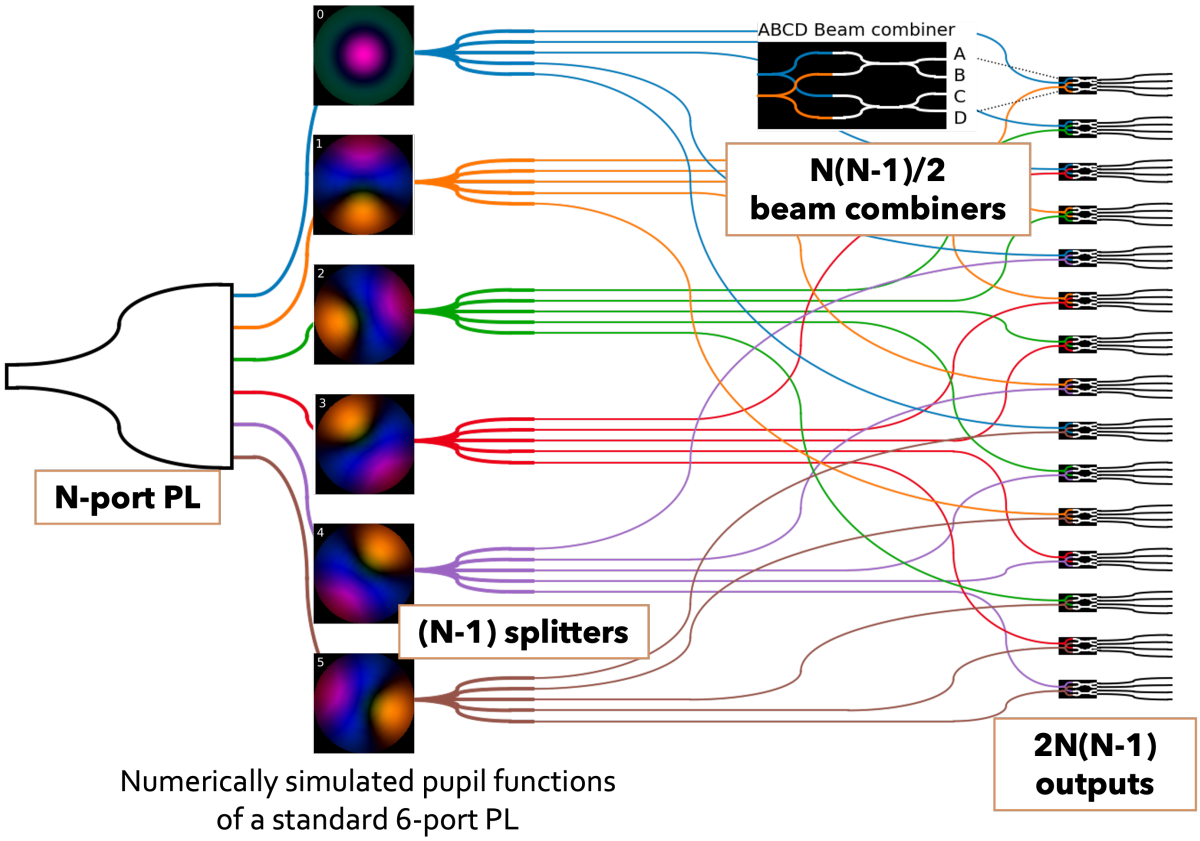

Figure 5. A conceptual diagram of a pairwise beam combiner for a 6-port PL. Light from each single-mode waveguide is split five ways, and each of these are directed to ABCD beam combiners in a pairwise manner. The intensity of outputs from ABCD beam combiners can be used to determine the visibilities.

cross-correlated PL pupil functions are extended and asymmetric, which is a deviation from normal aperture masking interferometry. The mutual intensity functions J_p at (u, v) coordinates other than the baseline defined by the blobs contribute to the PL visibilities and helps break position angle degeneracy.

Dependence of relative intensities on input scenes The relative intensities in the output SMFs depend on the source intensity distribution, unlike in conventional interferometry where differences in intensities are treated as an instrumental gain factor to be calibrated. Relative intensities in output SMFs are sensitive to low-order aberrations[4,6] which may be used to constrain source intensity distribution in addition to visibilities.

Limited field of view When coupling the telescope light into a PL at the focal plane, the field of view is determined by the size of the PL entrance diameter and the focal ratio. Any off-axis light that does not fall onto the FMF entrance will not couple into the PL. Note that the limited field of view also implies that the PL pupil functions are extended. In this simulation setup, the radius of the lantern entrance (FMF outer cladding radius) is about $1.5\lambda/D$. In Figure 6 (b) the PL squared visibilities converge to unity as the binary separation increases, indicating the limited field of view.

4. SIMULATED OBSERVATIONS AND POTENTIAL OF PL INTERFEROMETRY

In this section, we explore the potential of PL interferometry in the presence of photon noise and WFE. In subsection 4.1, we describe the methodology for simulating observations. Then we investigate the potential of PL

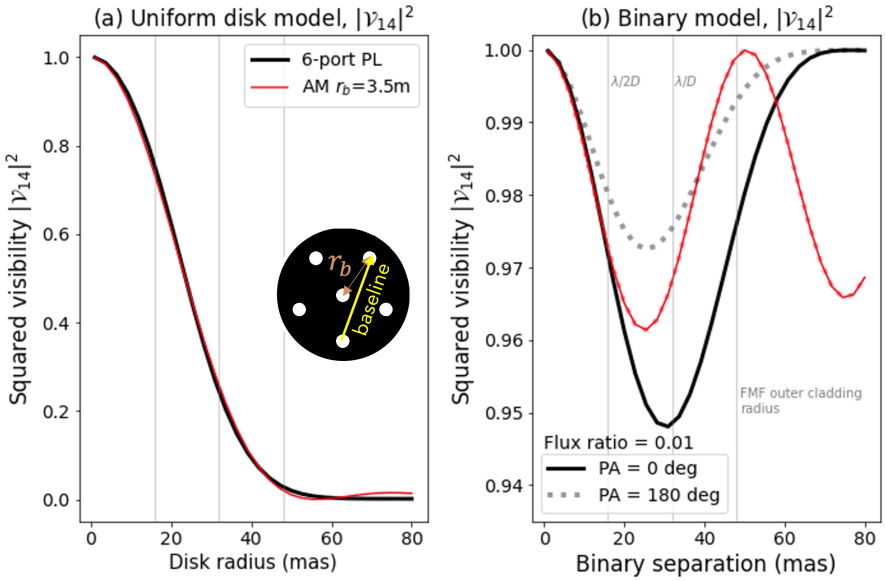

Figure 6. Simulated squared visibilities from modes 1 and 4, for PLs and aperture masking interferometry for simple models, (a) uniform circular disk and (b) binary with flux ratio 0.01 and two position angles 0 deg (solid lines) and 180 deg (dotted lines). In (b), the squared visibilities for 0 deg position angle and 180 deg position angle are different for PLs while they are degenerate for aperture masks. In average, PL visibilities agree well with the visibilities from aperture masking interferometry with $r_b = 3.4m$ at angular scales $< \lambda/2D$. PL visibilities are insensitive to scales larger than λ/D, as can be seen from visibilities approaching to unity as binary separation increases.

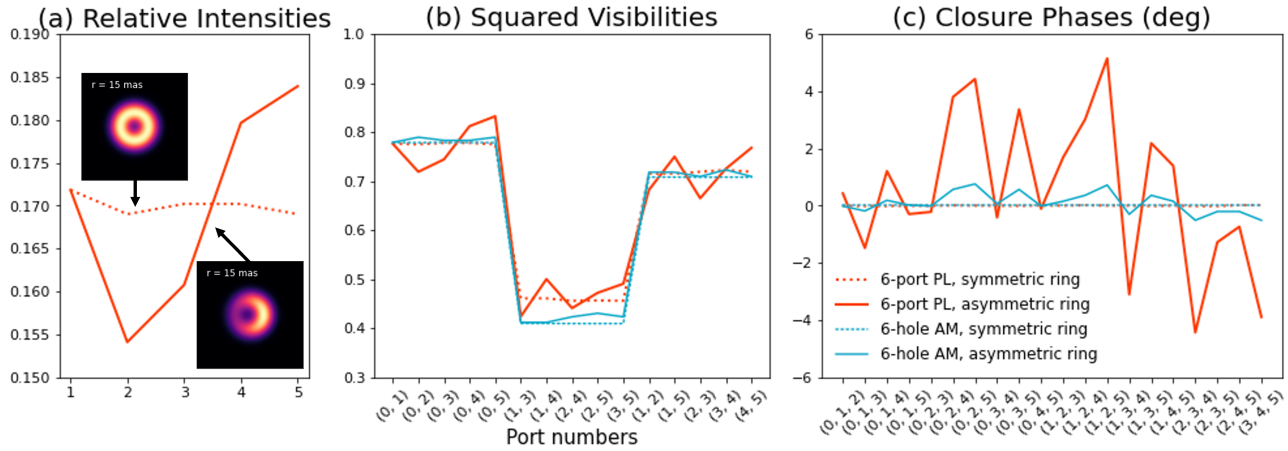

Figure 7. Simulated interferometric observables of a thin ring of 15 mas radius with central unresolved point source (nested figures in panel (a); convolved with a $\lambda/2D$ Gaussian beam for display), for symmetric case (dotted lines) and skew = 0.5 case (solid lines). Red lines and blue lines represent the case for PL interferometry and aperture masking interferometry, respectively. The differences in signals between the symmetric and the asymmetric case are more significant for the PL. The flux of the central point source (star) contributes to 50% of the total flux to the image but we only display the circumstellar components in the nested figures.

interferometry using simulated observations for two approaches: model fitting (subsection 4.2) and nonparametric image reconstruction (subsection 4.3).

4.1 Simulated observations

We consider a standard 6-port PL of which all SMFs have the same core refractive index and radius. We use a cladding index of 1.444, cladding-jacket index contrast of 5.5×10^{-3}, and core-cladding index contrast of

8.8×10^{-3}. Each SMF core diameter is chosen to be 4.4 μm and the FMF entrance diameter to be 10 μm. The lantern taper length is set to 2 cm and the taper scale (scale difference between the output and input ends) is set to 8. For the telescope, we use an unobstructed circular aperture with a 10 m diameter. The focal length is chosen to maximize the total coupling of an on-axis point source to all the supported LP modes, which gave a focal ratio of about 4.3. We used `lightbeam`[18] and `HCIPy`[19] python packages to simulate light propagation through the lantern and calculate effective apertures numerically. To simulate the effects of WFE, we generate 240 AO-corrected phase maps (average Strehl ratio = 0.65) over a period of 1 second and assign 120 of them to a calibrator (unresolved point source) observation and another 120 to the target observation. Therefore each observation consists of 120 exposures of 1 second target observation and 120 exposures of 1 second calibrator observation. We assume 25% combined throughput for the PL and the beam combiner, 50% for the coupling AO-corrected wavefront into the PL and 50% for the losses regarding the integrated optics beam combiner.

For comparison, we also simulate interferometric observables for aperture masks. For the throughput of aperture masks, we take the unfilled fraction of the telescope aperture, which results in 6% throughput for 1-m subapertures. This yields a throughput ratio of about 4:1 between PL and aperture masking interferometry. We employ the same simulation framework as the PL but substitute the PL pupil functions with aperture mask pupil functions. Therefore, the following comparison between the PL interferometry and aperture masking interferometry compares the consequence of having distinct pupil function geometries (extended lantern modes versus symmetric amplitude masks), yet might not capture the potential advantage of PL interferometry over classical aperture masks in terms of exploiting spatial filtering properties of PLs.

The interferometric observables are extracted from ABCD intensity outputs of each frame, including relative intensities, squared visibilities, and closure phases. The relative intensities are subtracted by the difference between the observed relative intensities of the calibrator star and the relative intensities for an unaberrated point source. The squared visibilities are divided and the closure phases are subtracted by those of the calibrator star's. Then the calibrated interferometric observables are averaged over the 120 exposures. These calibrated observables can be used as an input for parametric modeling (subsection 4.2) and non-parametric image reconstruction (subsection 4.3).

4.2 Parametric Modeling — A case for the Binary Model

We generate binary mock observations of various separations, contrasts, and position angles and fit the interferometric observables to models. Figure 8 shows contours of constant significance level (3σ) calculated on a grid of binary separation and contrast, for both the PL and the aperture mask. The significances computed as $\sigma = \sqrt{\chi^2_{\rm null} - \chi^2}$. In the photon noise-limited regime ($J = 19$ mag and $J = 14$ mag), PLs can reach greater contrast for a given separation compared to the aperture mask. This is because of the higher throughput of PLs than the aperture mask. In the WFE-limited regime ($J = 4$ mag) the significance levels are nearly equal. At separations larger than λ/D, the contrast limit decreases for PLs, reflecting decreased sensitivity due to the physical size of the FMF entrance at the focal plane. The contrast limit of the PL at small separations ($< \lambda/2D$) is slightly deeper than the aperture mask, owing to its greater sensitivity to the phase angle degeneracy.

4.3 Nonparametric Image Reconstruction

To test the potential of image reconstruction when using PL-measured visibilities, we run monochromatic image reconstruction simulations using the `squeeze` software[20] for ring models (Figure 7). `squeeze` uses the Markov Chain Monte Carlo (MCMC) algorithm with a simulated annealing technique to find the global maximum of the posterior. We modified the `squeeze` code to compute PL visibilities.

We generate mock data for symmetric and asymmetric ring models of three different radii (10 mas, 15 mas, and 25 mas) with unresolved star at the center as in Figure 7. We use the same turbulent phase screens as in Section 4.1 and the same calibration method. We set the total number of photons incident on the telescope aperture 10^{10} per exposure ($J = 4$ mag), so WFE dominates over the photon noise.

The middle and lower panels of Figure 9 show reconstructed images of environments of the central source, using the 6-port PL with beam combiners and 6-hole aperture masks ($r_b = 3.4m$), respectively. Although image reconstruction performance for the symmetric ring is similar for the PL and the aperture mask, PLs can recover asymmetries better than the aperture mask, as can be seen from the asymmetric ring cases. PL visibilities are

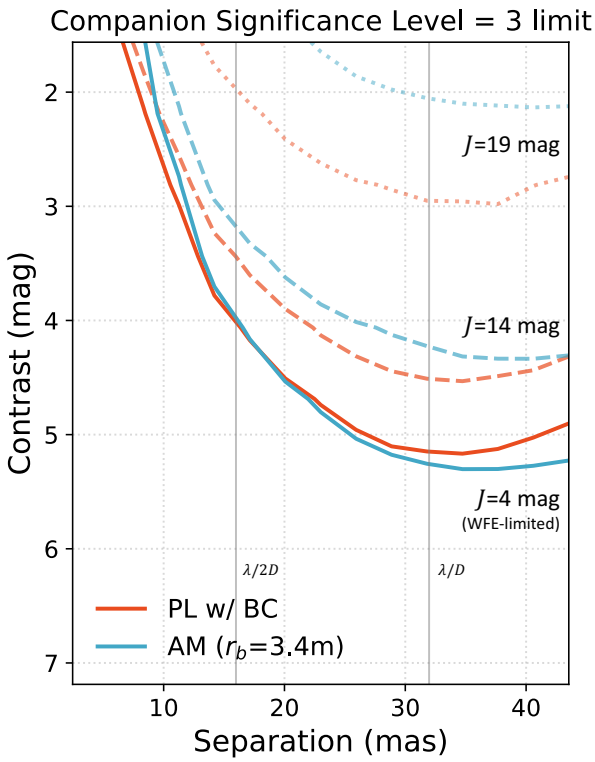

Figure 8. Contours showing significance level of 3σ for companion detection. The solid, dashed, and dotted lines correspond to the source brightness of $J = 4$ mag, $J = 14$ mag, and $J = 19$ mag, respectively. In photon-noise limited regime, throughput plays a major role in determining the significance levels, resulting in distinct curves between PLs and aperture masks.

sensitive to asymmetries even in small angular scales ($< \lambda/2D$), whereas the aperture mask can only partially recover asymmetries at larger angular scales (25 mas, $\sim \lambda/D$). This is expected from the larger signals of asymmetries for PLs than aperture masks depicted in Figure 7, especially the closure phases.

5. DISCUSSION

We presented a concept of using photonic lanterns for interferometric imaging and developed interferometric observables. The main benefits of PL interferometry found from simulated observations include 1) high throughput, leading to higher efficiency in the photon noise-limited regime compared to aperture masking interferometry, 2) sensitivity to low-order spatial features and asymmetries (especially at $< \lambda/2D$), and 3) spatial selectivity in crowded fields and reduced background noise due to the limited field of view.

Furthermore, the single-moded beams from the beam combiner outputs can be fed into a high-resolution spectrometer. This would enable high spectral resolution interferometric data and expand the detection limit to even smaller angular scales, using spectro-interferometry.[21] This may be cost-effective as it can be integrated with existing SMF-based spectrometers.

There are several complications to be addressed in future studies. The complex PL mode structures need to be accurately determined in the laboratory for precise model fitting and image reconstruction. The potential correlations in uncertainties in PL visibilities, caused by overlapping PL modes structures, should be examined to ensure accurate model fitting. Other practical complications include accounting for the variation in throughput of different PL outputs, balancing the intensities in beam combination, and dealing with chromaticity and polarization.

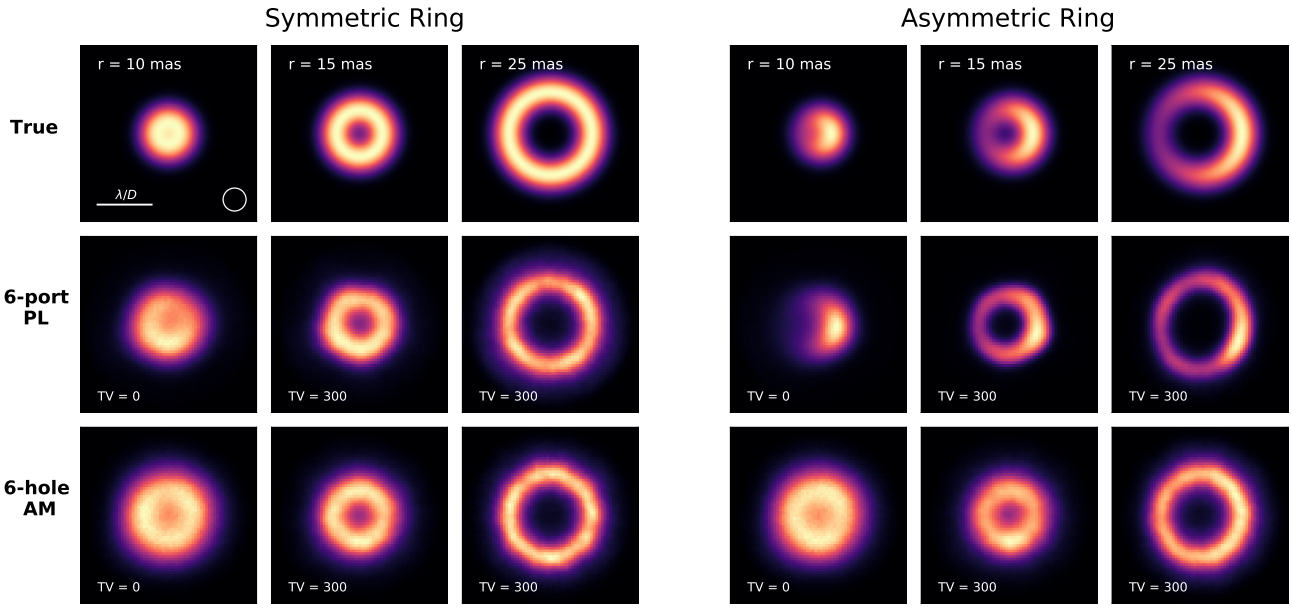

Figure 9. (Top) Ring models convolved with a beam of $\lambda/2D$ width. (Middle) Reconstructed images using `squeeze` with PL visibilities. (Bottom) Reconstructed images using `squeeze` with the aperture mask analog.

We considered using a photonic integrated circuit beam combiner to enable measurement of PL visibilities of a standard 6-port PL, but there are other designs and concepts that can be explored. Nulling interferometry may be performed to achieve a higher contrast by adjusting field amplitudes and phases, which is an addition to the concept of using a mode-selective PL for nulling on-axis starlight[9] or using a hybrid PL with a vortex mask.[22] Also, pairwise probing approach[23] with a PL can be explored to decompose coherent light (starlight) and incoherent light. If using an oversampled lantern of which the number of SMF outputs is larger than the number of supported modes, the SMF output intensities may contain interferometric information on the source and PL interferometry may be performed directly from SMF output intensities without a beam combiner. A larger mode count PL may provide increase Fourier coverage, a larger field of view, and a higher throughput, although larger complexity is expected if considering the pairwise beam combination scheme. Furthermore, different lantern geometry results in variations in lantern transfer matrices and thus the effective apertures,[22] which implies that design of the lantern may be optimized for interferometric imaging.

ACKNOWLEDGMENTS

This work is supported by the National Science Foundation under Grant No. 2109231 and No. 2109232.

REFERENCES

[1] Leon-Saval, S. G., Argyros, A., and Bland-Hawthorn, J., "Photonic lanterns," *Nanophotonics* **2**, 429–440 (Dec. 2013).

[2] Birks, T. A., Gris-Sánchez, I., Yerolatsitis, S., Leon-Saval, S. G., and Thomson, R. R., "The photonic lantern," *Advances in Optics and Photonics* **7**, 107 (June 2015).

[3] Jovanovic, N., Schwab, C., Cvetojevic, N., Guyon, O., and Martinache, F., "Enhancing Stellar Spectroscopy with Extreme Adaptive Optics and Photonics," **128**, 121001 (Dec. 2016).

[4] Lin, J., Fitzgerald, M. P., Xin, Y., Guyon, O., Leon-Saval, S., Norris, B., and Jovanovic, N., "Focal-plane wavefront sensing with photonic lanterns: theoretical framework," *Journal of the Optical Society of America B Optical Physics* **39**, 2643 (Oct. 2022).

[5] Norris, B. R. M., Wei, J., Betters, C. H., Wong, A., and Leon-Saval, S. G., "An all-photonic focal-plane wavefront sensor," *Nature Communications* **11**, 5335 (Oct. 2020).

[6] Kim, Y. J., Sallum, S., Lin, J., Xin, Y., Norris, B., Betters, C., Leon-Saval, S., Lozi, J., Vievard, S., Gatkine, P., Guyon, O., Jovanovic, N., Mawet, D., and Fitzgerald, M. P., "Spectroastrometry with photonic lanterns," in [*Ground-based and Airborne Instrumentation for Astronomy IX*], Evans, C. J., Bryant, J. J., and Motohara, K., eds., *Society of Photo-Optical Instrumentation Engineers (SPIE) Conference Series* **12184**, 1218449 (Aug. 2022).

[7] Levinstein, D. M., Sallum, S., Kim, Y. J., Lin, J., Fitzgerald, M. P., Lozi, J., Jovanovic, N., and Norris, B., "Spectro-astrometry of embedded accreting protoplanets using photonic lanterns," *Society of Photo-Optical Instrumentation Engineers (SPIE) Conference Series* **12680** (2023).

[8] Leon-Saval, S. G., Fontaine, N. K., Salazar-Gil, J. R., Ercan, B., Ryf, R., and Bland-Hawthorn, J., "Mode-selective photonic lanterns for space-division multiplexing," *Optics Express* **22**, 1036 (Jan. 2014).

[9] Xin, Y., Jovanovic, N., Ruane, G., Mawet, D., Fitzgerald, M. P., Echeverri, D., Lin, J., Leon-Saval, S., Gatkine, P., Kim, Y. J., Norris, B., and Sallum, S., "Efficient Detection and Characterization of Exoplanets within the Diffraction Limit: Nulling with a Mode-selective Photonic Lantern," **938**, 140 (Oct. 2022).

[10] Kim, Y. J., Fitzgerald, M. P., Lin, J., Sallum, S., Xin, Y., Jovanovic, N., and Leon-Saval, S., "Coherent Imaging with Photonic Lanterns," (submitted).

[11] Baldwin, J. E., Haniff, C. A., Mackay, C. D., and Warner, P. J., "Closure phase in high-resolution optical imaging," **320**, 595–597 (Apr. 1986).

[12] Haniff, C. A., Mackay, C. D., Titterington, D. J., Sivia, D., and Baldwin, J. E., "The first images from optical aperture synthesis," **328**, 694–696 (Aug. 1987).

[13] Tuthill, P. G., Monnier, J. D., Danchi, W. C., Wishnow, E. H., and Haniff, C. A., "Michelson Interferometry with the Keck I Telescope," **112**, 555–565 (Apr. 2000).

[14] Sallum, S. and Skemer, A., "Comparing nonredundant masking and filled-aperture kernel phase for exoplanet detection and characterization," *Journal of Astronomical Telescopes, Instruments, and Systems* **5**, 018001 (Jan. 2019).

[15] Shao, M. and Staelin, D. H., "Long-baseline optical interferometer for astrometry.," *Journal of the Optical Society of America (1917-1983)* **67**, 81–86 (Jan. 1977).

[16] Benisty, M., Berger, J. P., Jocou, L., Labeye, P., Malbet, F., Perraut, K., and Kern, P., "An integrated optics beam combiner for the second generation VLTI instruments," **498**, 601–613 (May 2009).

[17] Perraut, K., Jocou, L., Berger, J. P., Chabli, A., Cardin, V., Chamiot-Maitral, G., Delboulbé, A., Eisenhauer, F., Gambérini, Y., Gillessen, S., Guieu, S., Guerrero, J., Haug, M., Hausmann, F., Joulain, F., Kervella, P., Labeye, P., Lacour, S., Lanthermann, C., Lapras, V., Le Bouquin, J. B., Lippa, M., Magnard, Y., Moulin, T., Noël, P., Nolot, A., Patru, F., Perrin, G., Pfuhl, O., Pocas, S., Poulain, S., Scibetta, C., Stadler, E., Templier, R., Ventura, N., Vizioz, C., Amorim, A., Brandner, W., and Straubmeier, C., "Single-mode waveguides for GRAVITY. I. The cryogenic 4-telescope integrated optics beam combiner," **614**, A70 (June 2018).

[18] Lin, J., "Lightbeam: Simulate light through weakly-guiding waveguides." Astrophysics Source Code Library, record ascl:2102.006 (Feb. 2021).

[19] Por, E. H., Haffert, S. Y., Radhakrishnan, V. M., Doelman, D. S., Van Kooten, M., and Bos, S. P., "High Contrast Imaging for Python (HCIPy): an open-source adaptive optics and coronagraph simulator," in [*Adaptive Optics Systems VI*], *Proc. SPIE* **10703** (2018).

[20] Baron, F., Monnier, J. D., and Kloppenborg, B., "A novel image reconstruction software for optical/infrared interferometry," in [*Optical and Infrared Interferometry II*], Danchi, W. C., Delplancke, F., and Rajagopal, J. K., eds., *Society of Photo-Optical Instrumentation Engineers (SPIE) Conference Series* **7734**, 77342I (July 2010).

[21] Domiciano de Souza, A., Driebe, T., Chesneau, O., Hofmann, K. H., Kraus, S., Miroshnichenko, A. S., Ohnaka, K., Petrov, R. G., Preisbisch, T., Stee, P., Weigelt, G., Lisi, F., Malbet, F., and Richichi, A., "AMBER/VLTI and MIDI/VLTI spectro-interferometric observations of the B[e] supergiant CPD-572874. Size and geometry of the circumstellar envelope in the near- and mid-IR," **464**, 81–86 (Mar. 2007).

[22] Lin, J., Fitzgerald, M. P., Xin, Y., Kim, Y. J., Guyon, O., Leon-Saval, S., Norris, B., and Jovanovic, N., "Focal-plane wavefront sensing with photonic lanterns II: numerical characterization and optimization," (submitted).

[23] Give'on, A., Kern, B. D., and Shaklan, S., "Pair-wise, deformable mirror, image plane-based diversity electric field estimation for high contrast coronagraphy," in [*Techniques and Instrumentation for Detection of Exoplanets V*], Shaklan, S., ed., *Society of Photo-Optical Instrumentation Engineers (SPIE) Conference Series* **8151**, 815110 (Oct. 2011).